



## Effect of casting vacuum on thermodynamic and corrosion properties of Fe-based glassy alloy

Yi-min SUN, Yong-gang WANG, Ji-teng ZHANG, Rui LI, Ling-yu GUO, Hui XU, Wei-min WANG

Key Laboratory for Liquid-Solid Structural Evolution and Processing of Materials, Ministry of Education, Shandong University, Ji'nan 250061, China

Received 8 April 2014; accepted 13 June 2014

**Abstract:** The effect of casting vacuum on thermodynamic and corrosion properties of  $\text{Fe}_{61}\text{Co}_7\text{Zr}_8\text{Mo}_5\text{W}_2\text{B}_{17}$  in shape of cylinder of 3 mm in diameter and ribbon of 20–40  $\mu\text{m}$  in thickness and 2–3 mm in width were investigated with X-ray diffraction (XRD), differential scanning calorimetry (DSC), dilatometer (DIL), scanning electron microscopy (SEM) and electrochemical station. It is found that high casting vacuum can improve the glass forming ability (GFA), the contraction degree during heating, and the pitting resistance of the glassy alloy, which can be ascribed to the fact that the dissolution of tungsten in the melt is improved under the high casting vacuum.

**Key words:** Fe-based alloys; casting vacuum; dilation; corrosion resistance

### 1 Introduction

During the past few years, bulk metallic glasses (BMGs) have drawn increasing attention due to their remarkable properties including high strength, hardness, thermal stability and corrosion resistance [1–4]. As a member of BMG systems, Fe-based alloys are commercially the most important owing to not only much cheaper price than other BMGs, but also the unique combination of high mechanical, chemical and physical properties [5–8].

Since INOUE et al [9,10] discovered Fe–Co–(Zr, Nb, Ta)–(Mo, W)–B BMGs, more and more attention has been paid on them, especially on the  $\text{Fe}_{60}\text{Co}_{10}\text{Zr}_8\text{Mo}_5\text{W}_2\text{B}_{15}$  alloy due to its high glass-forming ability (GFA), excellent mechanical properties, high corrosion resistance and good soft magnetic properties. In recent years, the microstructure, GFA, fragility, viscosity, magnetic properties and crystallization kinetics of  $\text{Fe}_{61}\text{Co}_{9-x}\text{Zr}_8\text{Mo}_5\text{W}_x\text{B}_{17}$  ( $0 \leq x \leq 3$ ) glasses formed under different vacuum conditions have been investigated [11–14]. However, there are few investigations on the corrosion resistance of the Fe–Co–Zr–Mo–W–B alloys up to now.

In our earlier work, we have found that improving the casting vacuum can depress the formation of  $\text{ZrB}_2$  precipitation, and decrease the saturation magnetization of the as-cast Fe–Co–Zr–Mo–W–B glass [11]. However, different from the Fe–Co–Zr–Mo–W–B glass, the saturated magnetization of  $\text{Fe}_{78}\text{Si}_9\text{B}_{13}$  glass alloy does not change apparently with the casting vacuum. The corrosion potential  $\phi_{\text{corr}}$  and pitting start potential  $\phi_{\text{pit}}$  of  $\text{Fe}_{78}\text{Si}_9\text{B}_{13}$  glass alloy vary with changing the casting vacuum [15]. Hence, it is valuable to study the casting vacuum and corrosion behavior of the bulk Fe-based metallic glasses.

In Fe-based binary alloys, it is known that tungsten can decrease the expansion coefficient of the alloy [16]. In Fe-based glassy alloys, W is an important minor alloying element to improve the alloys' glass formability (GFA) [11]. Interestingly, analysis on the combination effect of tungsten and oxygen shows an optimal content value in searching the high GFA [12], which is often found in other Fe-based glassy systems [17]. Meanwhile, oxygen plays an important role in the structure, GFA and other properties of Fe-based alloys [15]. Hence, how does the casting vacuum affect the tungsten's role in glass forming is valuable to study.

Therefore, we choose  $\text{Fe}_{61}\text{Co}_7\text{Zr}_8\text{Mo}_5\text{W}_2\text{B}_{17}$  alloy

**Foundation item:** Project (51171091) supported by the National Natural Science Foundation of China; Project (JQ201012) supported by the Excellent Youth Project of Shandong Natural Science Foundation, China; Project (2012CB825702) supported by the National Basic Research Program of China

**Corresponding author:** Wei-min WANG; Tel: +86-531-88392749; FAX: +86-531-88395011; E-mail: [weiminw@sdu.edu.cn](mailto:weiminw@sdu.edu.cn)  
DOI: 10.1016/S1003-6326(15)63672-X

cast under different vacuum conditions, at last obtain cylinders of 3 mm in diameter and 50 mm in length and ribbons of 20–40  $\mu\text{m}$  in thickness and 2–3 mm in width. Subsequently, we investigate thermal stability, thermal expansion coefficient, corroded properties of  $\text{Fe}_{61}\text{Co}_7\text{Zr}_8\text{Mo}_5\text{W}_2\text{B}_{17}$  cylinders and ribbons formed under different vacuum conditions in 3.5% NaCl solution at 298 K open to air.

## 2 Experimental

The  $\text{Fe}_{61}\text{Co}_7\text{Zr}_8\text{Mo}_5\text{W}_2\text{B}_{17}$  cylinders used in this work were obtained by induction-melting the mixture of purity metals, except B that was added using a Fe–16.8%B master alloy. All ingots were re-molten at least three times to guarantee the uniform mixing of each element. In order to analyze the effect of vacuum on the amorphous Fe–Co–Zr–Mo–B alloy, the pressure of the casting chamber was reduced to  $2.0 \times 10^{-3}$  Pa with the mechanical vacuum pump and molecular vacuum pump, then input  $6 \times 10^4$  Pa argon before injection casting. Furthermore, we reduced vacuum of the casting chamber to  $2.0 \times 10^{-1}$  Pa with the mechanical vacuum pump only, and then  $6 \times 10^4$  Pa argon was input before injection casting. For the sake of clarity, the conditions with high and low casting vacuums are marked as HV and LV, respectively. Bulk cylinders were obtained by injection casting into copper moulds of 3 mm in diameter and 50 mm in length under different vacuum atmospheres. The  $\text{Fe}_{61}\text{Co}_7\text{Zr}_8\text{Mo}_5\text{W}_2\text{B}_{17}$  ribbons were prepared by a single-roller melt-spinning technique under different vacuum atmospheres. The diameter of the copper roller was 35 cm, and the circumferential speed  $R_c$  was 29.3 m/s. The ribbons were about 20–40  $\mu\text{m}$  in thickness and 2–3 mm in width. Since the cylinders may be inhomogeneous along cylinder axis, the middle part of the cylinders for the next investigations were chosen in order to equal the cooling conditions of alloys.

The phases in these samples were studied by X-ray diffraction (XRD) using a D/Max-rB diffractometer with Cu  $K_\alpha$  radiation. The microstructure and local compositions of these samples were studied by scanning electron microscope (SEM, HITACHI SU70) equipped with the energy dispersive X-ray spectrometer (EDS). The thermal behaviors of samples were examined using the differential scanning calorimeter (Netzsch DSC 404c) under an argon atmosphere at a heating rate of 20 K/min. The dilatation measurements were conducted with a conventional dilatometer (Netzsch DIL 402C) at a heating rate of 10 K/min for the cylinder samples only. Here, the expansion coefficient of the cylinder in glassy state was calculated by average differential value of the linear part of dilation curve.

LK 2005A electrochemical workstation was used

for the polarization curves. Corrosion resistance was evaluated by potentiodynamic polarization measurement using a three-electrode cell. The working electrode corresponded to the tested alloy, the counter electrode was a platinum sheet and the reference electrode was a saturated calomel electrode. Potentiodynamic curves were performed at a scan rate of 0.01 V/s in 3.5% NaCl solution at 298 K open to air.

## 3 Results and discussion

### 3.1 XRD patterns of $\text{Fe}_{61}\text{Co}_7\text{Zr}_8\text{Mo}_5\text{W}_2\text{B}_{17}$ samples

Figure 1 shows the X-ray diffraction (XRD) patterns of  $\text{Fe}_{61}\text{Co}_7\text{Zr}_8\text{Mo}_5\text{W}_2\text{B}_{17}$  cylinders and ribbons under HV and LV conditions, which present a typical amorphous broad diffraction peak together with the crystalline peaks. For cylinder with HV condition, the crystalline peaks are identified as  $\alpha$ -Fe,  $\text{Fe}_{23}\text{Zr}_6$  and  $\text{Fe}_3\text{B}$ ; for the cylinder with LV, the peaks include  $\alpha$ -Fe,  $\text{Fe}_3\text{B}$ ,  $\text{ZrB}_2$ , WB, and  $\text{CoW}_2\text{B}_2$ . In XRD patterns of the ribbon with HV, only a typical amorphous broad diffraction peak exists, indicating a fully amorphous structure; but with LV, the peaks include  $\alpha$ -Fe and  $\text{ZrB}_2$ . Apparently, the glass phase fraction of cylinder and ribbon under HV is much higher than that under LV, implying that increasing the vacuum is helpful to improving the glass forming ability (GFA) of the alloy.

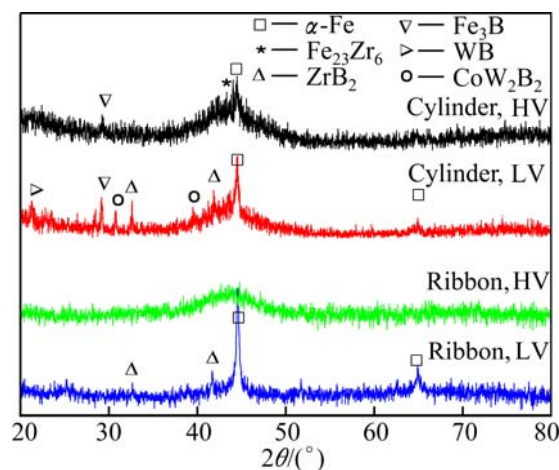


**Fig. 1** XRD patterns of  $\text{Fe}_{61}\text{Co}_7\text{Zr}_8\text{Mo}_5\text{W}_2\text{B}_{17}$  cylinders and ribbons under different vacuum conditions

### 3.2 DSC and dilation measurements of $\text{Fe}_{61}\text{Co}_7\text{Zr}_8\text{Mo}_5\text{W}_2\text{B}_{17}$ samples

Figure 2 gives the DSC analysis results of  $\text{Fe}_{61}\text{Co}_7\text{Zr}_8\text{Mo}_5\text{W}_2\text{B}_{17}$  cylinders and ribbons under different vacuum conditions at a heating rate of 20 K/min. In curves of cylinders, there are two and three exothermic peaks with HV and LV, respectively. The total area of the exothermic peaks with HV is higher than that with LV, which is consistent with XRD patterns in

Fig. 1. In DSC curves of ribbons, there is an unclear exothermic peak for the ribbon with LV, suggesting a low glass fraction in the ribbon, which is consistent with the XRD patterns (Fig. 1). Meanwhile, the primary crystallization of  $\alpha$ -Fe of the ribbons is earlier than the cylinder samples.

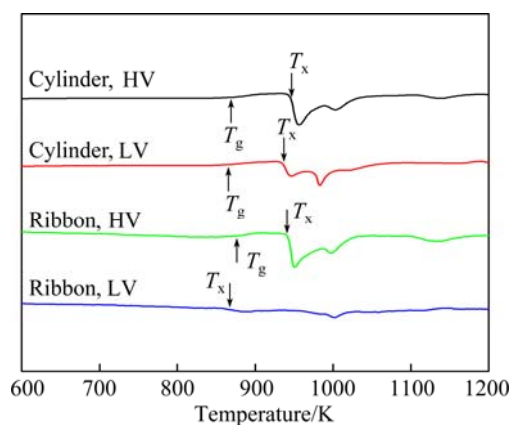


**Fig. 2** DSC curves of  $\text{Fe}_{61}\text{Co}_7\text{Zr}_8\text{Mo}_5\text{W}_2\text{B}_{17}$  cylinders and ribbons under different vacuum conditions at heating rate of 20 K/min

Figure 3 shows the thermal expansion curves of cylinder samples at a heating rate of 10 K/min. In the range of 500–1200 K, the curves can be divided into three parts, which are labeled as stage I, II and III, respectively. Obviously, the slope of the curves of two cylinders at stage I is similar to each other; and both cylinder samples present a contraction at stage II. Here, the start temperature ( $T_d$ ) of stage II, the contraction degree ( $\delta$ ) as well as the glass transition temperature ( $T_g$ ), and the onset of first crystallization ( $T_x$ ) are shown in Table 1.

As indicated in Table 1,  $\delta$  of cylinders equals the difference between thermal expansion value  $dL/L_0$  of stage I and the extrapolated  $dL/L_0$  of stage III at  $T_d$ . It is

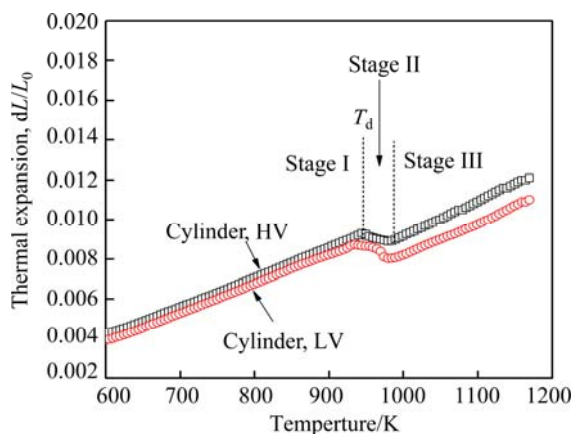


**Fig. 3** Thermal expansion curves of  $\text{Fe}_{61}\text{Co}_7\text{Zr}_8\text{Mo}_5\text{W}_2\text{B}_{17}$  cylinders under different vacuum conditions at heating rate of 10 K/min

**Table 1** Thermal and dilation parameters of  $\text{Fe}_{61}\text{Co}_7\text{Zr}_8\text{Mo}_5\text{W}_2\text{B}_{17}$  cylinders ( $d3$  mm) and ribbons with various casting vacuum conditions

Sample	$T_g/\text{K}$	$T_x/\text{K}$	$T_d/\text{K}$	$\alpha_l/10^6\text{K}^{-1}$	$\delta$
Cylinder, HV	892	942	942	14.92	0.0011
Cylinder, LV	881	935	932	14.55	0.0016
Ribbon, HV	562	933			
Ribbon, LV	–	863			

found that  $T_g$  and  $T_x$  of cylinder sample with HV are higher than those with LV, indicating that it can improve thermal stability by improving the casting vacuum.  $T_d$  is similar to the corresponding value of  $T_x$ , indicating that the contraction for the cylinder samples in Fig. 3 results from the crystallization processes [18].  $\delta$  of the cylinder with HV is lower than that with LV, although the amorphous phase fraction of the former is higher than that of the latter (Fig. 1). This indicates that the packing density of cylinder with HV is higher than that with LV, which accords with their GFA shown in Fig. 1 and the density argument that the alloy with a higher packing density has a higher GFA [19,20].

### 3.3 Electrochemical behavior of $\text{Fe}_{61}\text{Co}_7\text{Zr}_8\text{Mo}_5\text{W}_2\text{B}_{17}$ samples

Figure 4 shows potentiodynamic polarization curves of  $\text{Fe}_{61}\text{Co}_7\text{Zr}_8\text{Mo}_5\text{W}_2\text{B}_{17}$  cylinders and ribbons under different vacuum conditions in 3.5% NaCl solution at 298 K open to air. For the cylinder samples, there exist two passivation regions while the passivation characteristics are changed for the ribbon samples. In polarization curves of cylinder samples, the first peak starts at  $\phi_{\text{mpit}}$  which can be considered metastable pitting process. The current peak is consistent with the peak induced by micro-cracking in the Al-based glasses [21]. The rise of current density ( $J$ ) at  $\phi_{\text{spit}}$  indicates the occurrence of the stable pitting process. The corrosion

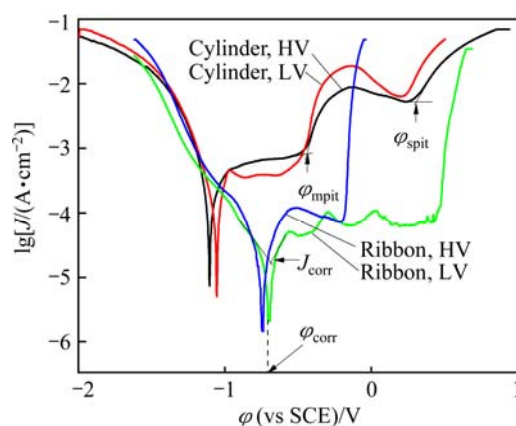


**Fig. 4** Potentiodynamic polarization curves of  $\text{Fe}_{61}\text{Co}_7\text{Zr}_8\text{Mo}_5\text{W}_2\text{B}_{17}$  cylinders and ribbons under different vacuum conditions in 3.5% NaCl solution at 298 K open to air

potential  $\phi_{\text{corr}}$  of cylinder samples is more negative than that of ribbon samples. Generally, the more negative corrosion potential means a worse corrosion resistance and the sample with a higher amorphous fraction has a higher corrosion resistance [22], so it is expected that the ribbons consist of a larger amorphous fraction and possess a better corrosion resistance for electrochemical test. However, the ribbon with LV has a very low amorphous fraction, but a high  $\phi_{\text{corr}}$ . This result may be due to another factor affecting the  $\phi_{\text{corr}}$  of samples and valuable to further study.

In order to analyze the details of polarization of samples, the involved electrochemical parameters such as corrosion potential ( $\phi_{\text{corr}}$ ), metastable and stable pitting potentials ( $\phi_{\text{mpit}}$ ,  $\phi_{\text{spit}}$ ), and corrosion and passive current densities ( $J_{\text{corr}}$  and  $J_{\text{pass}}$ ) are listed in Table 2. Here, the  $\phi_{\text{corr}}$  of both cylinder samples is similar to each other, and the  $J_{\text{corr}}$  and  $J_{\text{pass}}$  of sample with HV are higher than those with LV. Meanwhile, the  $\phi_{\text{mpit}}$  and  $\phi_{\text{spit}}$  of cylinder with HV are higher than those with LV, indicating that increasing the vacuum can improve the pitting resistance of the cylinders. For the ribbons, the  $\phi_{\text{spit}}$  with HV is much higher than that with LV,

suggesting that the stability of the passive film is drastically improved by increasing the casting vacuum. In other words, improving the vacuum condition can strengthen the corrosion resistance of the passive process.

**Table 2** Electrochemical parameters of  $\text{Fe}_{61}\text{Co}_{9-x}\text{Zr}_8\text{Mo}_5\text{W}_x\text{B}_{17}$  cylinders and ribbons with different vacuum conditions in 3.5% NaCl solution

Sample	$\phi_{\text{corr}}/\text{V}$	$\lg[J_{\text{corr}}/(\text{A}\cdot\text{cm}^{-2})]$	$\lg[J_{\text{pass}}/(\text{A}\cdot\text{cm}^{-2})]$	$\phi_{\text{mpit}}/\text{V}$	$\phi_{\text{spit}}/\text{V}$
Cylinder, HV	-1.10	-3.5	-3.1	-0.43	0.31
Cylinder, LV	-1.05	-3.7	-3.4	-0.50	0.23
Ribbon, HV	-0.705	-4.7	-4.1	-	0.46
Ribbon, LV	-0.740	-4.5	-4.1	-	-0.17

### 3.4 Morphologies of immersed $\text{Fe}_{61}\text{Co}_7\text{Zr}_8\text{Mo}_5\text{W}_2\text{B}_{17}$ cylinders

To better understand the corrosion characteristic of the  $\text{Fe}_{61}\text{Co}_7\text{Zr}_8\text{Mo}_5\text{W}_2\text{B}_{17}$  alloy, the immersion experiment was performed on the cylinder samples with HV and LV and the SEM images are shown in Fig. 5.

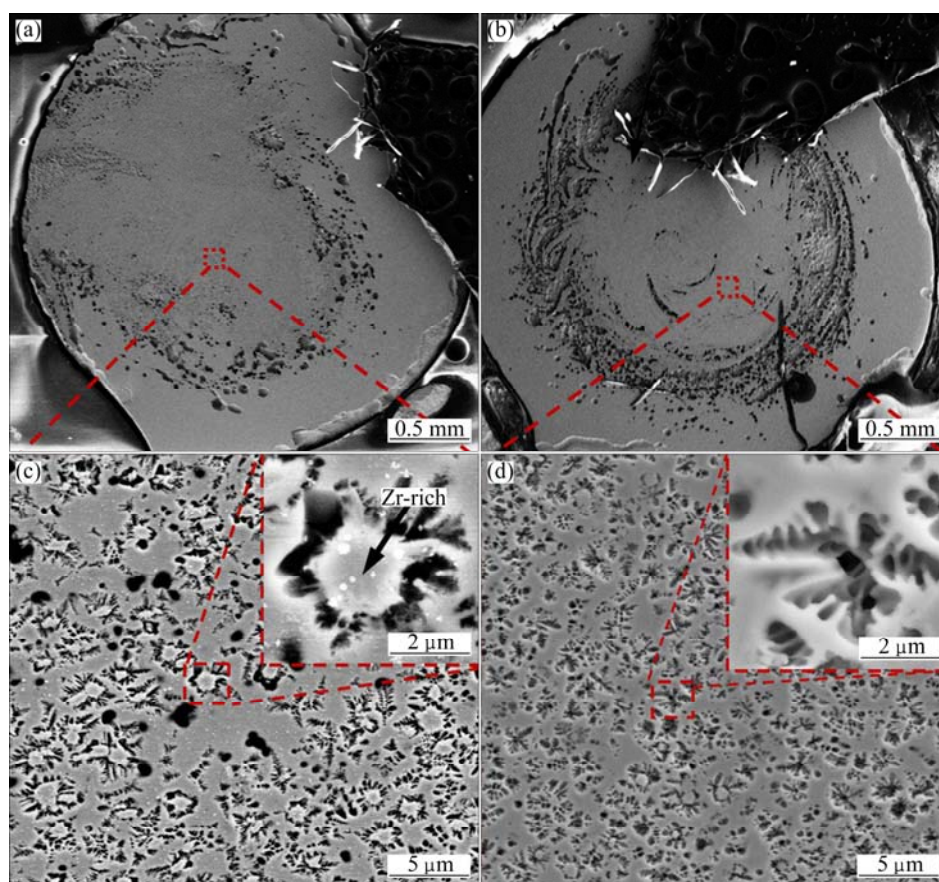


**Fig. 5** SEM images of corroded surfaces of  $\text{Fe}_{61}\text{Co}_7\text{Zr}_8\text{Mo}_5\text{W}_2\text{B}_{17}$  cylinders ( $d3$  mm) after 1 h immersion in 3.5% NaCl solution at 298 K open to air: (a) Macroscopic picture of immersed cylinder sample with high vacuum; (b) Macroscopic picture of immersed cylinder sample with low vacuum; (c) SEM image of film matrix of immersed cylinder sample with high vacuum; (d) SEM image of film matrix of immersed cylinder sample with low vacuum (Insets are magnification of morphology of the corroded phase)

Both cylinder samples are immersed in 3.5% NaCl solution at 298 K open to air for 1 h. A lot of pits of 2–5  $\mu\text{m}$  in diameter distribute toroidally in the cross section of the cylinder with HV (Fig. 5(a)). The cylinder with LV has more corrosion pits distributing toroidally (Fig. 5(b)), indicating the worse corrosion resistance of the alloy.

In magnified images (Figs. 5(c) and (d)), the pits appear in dendritic shape, which should be the trace left by dissolving  $\alpha\text{-Fe}$ , according to the size and shape of precipitated  $\alpha\text{-Fe}$  in our earlier work [11]. In the cylinder with HV, the dendritic pit is adhered on one block phase and forms a core-shell structure. The core is Zr-rich by EDS analysis. In the cylinder with LV, the number of core-shell structures is lower than that in the cylinder with HV, and the number of pure dendritic pits is higher. In other words, during the immersion, the pitting processes more smoothly in cylinder with LV than with HV, according with its lower  $\phi_{\text{spit}}$  (Table 2).

The compositions of matrix and center part of the dendrites of both cylinders by EDS analysis are shown in Table 3. Here, the oxygen content in matrix and dendrite core of the cylinder with HV is lower than that with LV. This suggests that the oxidation of the cylinder with LV is heavier than the cylinder with HV, namely, the cylinder with LV has a lower oxidation resistance than that with HV, also being consistent with their  $\phi_{\text{spit}}$  (Table 2). In addition, the tungsten content of the cylinder with HV is higher than that with LV (Table 3). It is known that tungsten can decrease the expansion coefficient of the Fe-based binary alloy [16]. Hence, it is expected that the contraction degree ( $\delta$ ) of sample with HV is lower than that with LV (Fig. 3). Meanwhile, the WB is found in the cylinder with LV, but is absent in that with HV (Fig. 1). Inside a cylinder, the bubble can drive the liquid flowing in a toroidal velocity distribution [23], which can be also caused by convections [24,25]. Hence, the W leant in the cylinder with LV can be ascribed to the fact that WB precipitates peel off during immersion or that WB has not dissolved into the melt and has segregated along the toroidal trace to the slug/riser by convections. As earlier literature mentioned [26], W can improve the pitting potential of the special steel. Accordingly, it is expected that the  $\phi_{\text{spit}}$  of the cylinder with HV is higher than that with LV (Table 2).

**Table 3** EDS analysis of immersed  $\text{Fe}_{61}\text{Co}_{9-x}\text{Zr}_8\text{Mo}_5\text{W}_x\text{B}_{17}$  cylinders with different vacuums in 3.5% NaCl solution

Sample	Position	$x/\%$						
		Fe	Co	Zr	Mo	W	B	O
Cylinder, HV	Matrix	48.2	6.0	6.9	4.8	1.5	22.2	10.2
	Pit center	43.9	5.5	8.3	4.7	1.4	23.7	11.9
Cylinder, LV	Matrix	39.9	5.4	7.9	4.5	0.7	19.6	20.3
	Pit center	46.3	6.6	7.9	4.5	0.7	16.6	15.9

In Fe-based glassy alloys, the tri-capped triangular prisms with Fe–B bonds can easily form the net-like structure [27,28]. The large and small atoms can form the strong backbone structure clusters in metallic glasses [29], especially in Al-based glasses [30]. Under LV condition, Zr and W atoms tend to form boride and precipitate out from the melt (Fig. 1) and should weaken the backbone clusters in the glass. Hence, it is expected that the cylinder with LV shows a worse corrosion resistance than that with HV (Fig. 4). In other words, increasing the casting vacuum can improve the dissolution of W and Zr into the melt, enhance the formation of the backbone clusters, and finally improve the GFA and corrosion resistance of Fe-based alloys.

## 4 Conclusions

1) Increasing vacuum degree can improve the glassy formability, thermal stability and expansion coefficient, and the corrosion resistance of the Fe-based glassy alloy.

2) The advantages of increasing the casting vacuum can be ascribed to the fact that the W and Zr dissolve more easily into the melt under the higher vacuum condition.

## References

- [1] JOHNSON W L. Bulk glass-forming metallic alloys: Science and technology [J]. MRS Bulletin, 1999, 24(10): 42–56.
- [2] SHEN T D, SCHWARZ R B. Bulk ferromagnetic glasses prepared by flux melting and water quenching [J]. Applied Physics Letters, 1999, 75(1): 49–51.
- [3] ZHANG Yang-huan, YANG Tai, BU Wen-gang, CAI Ying, ZHANG Guo-fang, ZHAO Dong-liang. Effect of Nd content on electrochemical performances of nanocrystalline and amorphous  $(\text{Mg}_{24}\text{Ni}_{10}\text{Cu}_2)_{100-x}\text{Nd}_x$  ( $x=0\text{--}20$ ) alloys prepared by melt spinning [J]. Transactions of Nonferrous Metals Society of China, 2013, 23(12): 3668–3676.
- [4] XU Hong-wei, DU Yu-lei, DENG Yu. Effects of Y addition on structural and mechanical properties of CuZrAl bulk metallic glass [J]. Transactions of Nonferrous Metals Society of China, 2012, 22(4): 842–846.
- [5] WANG Shan-lin, CHENG Jiang-chang, YI Seong-Hoon, KE Li-ming. Corrosion resistance of Fe-based amorphous metallic matrix coating fabricated by HVOF thermal spraying [J]. Transactions of Nonferrous Metals Society of China, 2014, 24(1): 146–151.
- [6] SHEN T D, SCHWARZ R B. Lowering critical cooling rate for forming bulk metallic glass [J]. Applied Physics Letters, 2006, 88: 091903-01–3.
- [7] GUO Sheng-feng, WANG Jing-feng, ZHANG Hong-ju, XIE Sheng-hui. Enhanced plasticity of Fe-based bulk metallic glass by tailoring microstructure [J]. Transactions of Nonferrous Metals Society of China, 2012, 22(2): 348–353.
- [8] WANG Y B, LI H F, ZHENG Y F, LI M. Corrosion performances in simulated body fluids and cytotoxicity evaluation of Fe-based bulk metallic glasses [J]. Materials Science and Engineering C, 2012, 32(3): 599–606.
- [9] INOUE A, ZHANG T, KOSHIBA H, MAKINO A. New bulk amorphous Fe–(Co, Ni)–M–B (M= Zr, Hf, Nb, Ta, Mo, W) alloys

- with good soft magnetic properties [J]. *Journal of Applied Physics*, 1998, 83(11): 6326–6328.
- [10] INOUE A, WANG X M. Bulk amorphous FC20 (Fe–C–Si) alloys with small amounts of B and their crystallized structure and mechanical properties [J]. *Acta Materialia*, 2000, 48(6): 1383–1395.
- [11] WANG W M, GEBERT A, ROTH S, KUEHN U, SCHULTZ L. Glass formability and fragility of  $\text{Fe}_{61}\text{Co}_{9-x}\text{Zr}_8\text{Mo}_5\text{W}_x\text{B}_{17}$  ( $x=0$  and  $2$ ) bulk metallic glassy alloys [J]. *Intermetallics*, 2008, 16(2): 267–272.
- [12] ZHANG J T, WANG W M, MA H J, LI R, ZHANG Z H. Isochronal and isothermal crystallization kinetics of amorphous Fe-based alloys [J]. *Thermochimica Acta*, 2010, 505(1): 41–46.
- [13] WANG W M, ZHANG W X, GEBERT A, ROTH S, MICKEL C, SCHULTZ L. Microstructure and magnetic properties in  $\text{Fe}_{61}\text{Co}_{9-x}\text{Zr}_8\text{Mo}_5\text{W}_x\text{B}_{17}$  ( $0 \leq x \leq 3$ ) glasses and glass-matrix composites [J]. *Metallurgical and Materials Transactions A*, 2009, 40(3): 511–521.
- [14] WANG W M, ZHANG J T, GEBERT A, ROTH S, SCHULTZ L. Casting vacuum effects on the precipitates and magnetic properties of Fe-based glassy alloys [J]. *Journal of Non-Crystalline Solids*, 2011, 357(7): 1657–1664.
- [15] MENG L L, LI X Y, PANG J, WANG L, AN B, YIN L J, SONG K K, WANG W M. Casting atmosphere effects on the precipitates magnetism, and corrosion resistance of  $\text{Fe}_{78}\text{Si}_9\text{B}_{13}$  glassy alloys [J]. *Metallurgical and Materials Transactions A*, 2013 11(44): 5122–5133.
- [16] LI Qing-chun. *Forming foundation of castings* [M]. Beijing: Chinese Mechanical Press, 1982: 182. (in Chinese)
- [17] CHIN T S, LIN C Y, LEE M C, HUANG R T, HUANG S M. Bulk nano-crystalline Fe-based alloys by annealing bulk glassy precursors [J]. *Intermetallics*, 2008, 16(1): 52–57.
- [18] SHEK C H, LIN G M. Dilatometric measurements and calculation of effective pair potentials for  $\text{Zr}_{41}\text{Ti}_{14}\text{Cu}_{12.5}\text{Ni}_{10}\text{Be}_{22.5}$  bulk metallic glass [J]. *Materials Letters*, 2003, 57(5): 1229–1232.
- [19] LI Y, GUO Q, KALB J A, THOMPSON C V. Matching glass-forming ability with the density of the amorphous phase [J]. *Science*, 2008, 322(5909): 1816–1819.
- [20] MA H J, ZHANG J T, LI G H, ZHANG W X, WANG W M. Effect of Zr on the thermal stability and magnetic properties of  $\text{Fe}_{78}\text{Si}_9\text{B}_{13}$  glassy alloy [J]. *Journal of Alloys and Compounds*, 2010, 501: 227–232.
- [21] LI G H, PAN S P, QIN J Y, ZHANG Z H, WANG W M. Insight into thermodynamics and corrosion behavior of Al–Ni–Gd glassy alloys from atomic structure [J]. *Corrosion Science*, 2013, 66: 360–368.
- [22] ARCHER M D, CORKER C C, HARJI B H. The electrochemical properties of metallic glasses [J]. *Electrochim Acta*, 1987(32): 13–26.
- [23] MIAO X, LUCAS D, REN Z, ECKERT S, GERBETH G. Numerical modeling of bubble-driven liquid metal flows with external static magnetic field [J]. *International Journal of Multiphase Flow*, 2013, 48: 32–45.
- [24] NIKRITYUK P A, ECKERT K, GRUNDMANN R. A numerical study of unidirectional solidification of a binary metal alloy under influence of a rotating magnetic field [J]. *International Journal of Heat and Mass Transfer*, 2006, 49(7): 1501–1515.
- [25] ŠVEC O, SKOČEK J, STANG H, GEIKER M R, ROUSSEL N. Free surface flow of a suspension of rigid particles in a non-Newtonian fluid: A lattice Boltzmann approach [J]. *Journal of Non-Newtonian Fluid Mechanics*, 2012, 179: 32–42.
- [26] AHN M K, KWON H S, LEE H M. Quantitative comparison of the influences of tungsten and molybdenum on the passivity of  $\text{Fe}_{29}\text{Cr}$  ferritic stainless steels [J]. *Corrosion Science*, 1998, 40(2): 307–322.
- [27] GASKELL P H. A new structural model for amorphous transition metal silicides, borides, phosphides and carbides [J]. *Journal of Non-Crystalline Solids*, 1979, 32: 207–224.
- [28] MA H J, WANG W M, PAN S P, CAO C D, ZHANG H D. Role of net-like zones on the crystallization behavior and soft magnetic property of  $\text{Fe}_{72}\text{Y}_6\text{B}_{23}$  glassy alloy [J]. *Sci Sin: Phys, Mech & Astron*, 2012, 42: 583–591.
- [29] POON S J, SHIFLET G J, GUO F Q, PONNAMBALLAM V. Glass formability of ferrous-and aluminum-based structural metallic alloys [J]. *Journal of Non-Crystalline Solids*, 2003, 317(1): 1–9.
- [30] LIU Y, YE S L, AN B, WANG Y G, LI Y J, ZHANG L C, WANG W M. Effects of mechanical compression and autoclave treatment on the backbone clusters in the  $\text{Al}_{86}\text{Ni}_9\text{La}_5$  amorphous alloy [J]. *Journal of Alloys and Compounds*, 2014, 587: 59–65.

## 铸造真空度对铁基非晶热力学和腐蚀行为的影响

孙益民, 王永刚, 张集滕, 李瑞, 郭玲玉, 徐慧, 王伟民

山东大学 材料液固结构演变与加工教育部重点实验室, 济南 250061

**摘要:** 采用 X 射线衍射(XRD)、差示扫描量热仪(DSC)、热膨胀仪(DIL)、扫描电子显微镜(SEM)和电化学工作站研究铸造气氛对  $\text{Fe}_{61}\text{Co}_9\text{Zr}_8\text{Mo}_5\text{W}_2\text{B}_{17}$  合金棒(直径为 3 mm)的热力学和腐蚀特性的影响。研究发现, 高的铸造真空度能够提高合金的非晶形成能力、加热时的收缩程度和点蚀抗性。这些性能的改善归因于高的铸造真空度能够提高钨在合金熔体中的溶解能力。

**关键词:** 铁基合金; 铸造真空度; 热膨胀; 耐腐蚀性

(Edited by Xiang-qun LI)